Journal of Alloys and Compounds 586 (2014) 616–620

Contents lists available at ScienceDirect

Journal of Alloys and Compounds

journal homepage: www.elsevier.com/locate/jalcom

Deformation mechanisms in ultrahigh-strength and high-ductility nanostructured FeMnAlC alloy

Chih-Lung Lin [a], Chuen-Guang Chao [a], Jenh-Yih Juang [b], Jenn-Ming Yang [c], Tzeng-Feng Liu [a,*]

[a] Department of Materials Science and Engineering, National Chiao Tung University, Hsinchu, Taiwan
[b] Department of Electrophysics, National Chiao Tung University, Hsinchu, Taiwan
[c] Department of Materials Science and Engineering, University of California, Los Angels, CA, USA

ARTICLE INFO

Article history:
Received 26 August 2013
Received in revised form 16 October 2013
Accepted 19 October 2013
Available online 28 October 2013

Keywords:
Metals and alloys
Nanostructured materials
Lightweight alloy
Spinodal decomposition
Bursting dislocation nucleation
Taylor lattice

ABSTRACT

The deformation mechanisms of a bulk nanostructured Fe–30Mn–9.5Al–2.0C (in wt.%) alloy were investigated. After aging at 450 °C for 9–12 h, the alloy exhibits an exceptional strength-ductility combination (e.g. yield strength ~1406 MPa with elongation ~32%). The aged alloy exhibits a novel microstructure with isolated austenite nano-channels bounded by an extremely high volume fraction of directional nano-sized $(Fe,Mn)_3AlC$ carbides (κ′-carbides). The plastic deformation was found to be dominated by bursting dislocation nucleation within the isolated austenite nano-channels.

1. Introduction

Lightweight Fe–Mn–Al–C alloys with excellent combination of strength and ductility are promising candidate for automobile structural applications [1]. The microstructural evolution and mechanical properties of fully austenitic Fe–Mn–Al–C alloys have been extensively studied. Previous results showed that the as-quenched microstructure of Fe–(28–30.5)Mn–(7.8–10)Al–(0.8–1.3)C (in wt.%) alloys was single-phase austenite (γ) [2–5]. After being optimally aged (550 °C, 15–16 h), a high density of nano-sized $(Fe,Mn)_3AlC$ carbides (κ′-carbides) having an ordered $L'1_2$ structure started to precipitate coherently within the γ matrix and no precipitates were formed on the grain boundaries. The resulting microstructure led to a very good combination of strength and ductility with an elongation (El) better than about 30%, values of 1120–1259 MPa for ultimate tensile stress (UTS) and 1080–1094 MPa for yield strength (YS) could be attained [2,3]. The strengthening mechanisms to account for the excellent strength-ductility combination were attributed to the precipitation of shearable nano-sized κ′-carbides and the substructures associated with planar glide (such as Taylor lattice, Taylor lattice domain boundaries and microbands) [4,5].

Recently, we observed an interesting microstructural feature in the as-quenched Fe–Mn–Al–C alloys with higher carbon content: an extremely high density of nano-sized κ′-carbides was formed within the γ matrix by spinodal decomposition during quenching [6–9]. The amount of nano-sized κ′-carbides increased with increasing carbon content [9]. The unique κ′-carbides formation mechanism is quite different from that occurred in the Fe–Mn–Al–C ($C \leqslant 1.3$) alloys, wherein the nano-sized κ′-carbides could only be observed in the aged alloys [2–5]. Due to the pre-existing nano-sized κ′-carbides in the as-quenched alloys, both the aging temperature and aging time required for attaining the optimal combination of strength and ductility could be dramatically reduced. Furthermore, after being properly aged, the alloys have far superior combination of strength and ductility to that of the Fe–Mn–Al–C ($C \leqslant 1.3$) alloys. For example, with almost equivalent elongation, the Fe–28Mn–9Al–1.8C alloy aged at 450 °C for 12 h could possess 28% higher YS than that of the optimally aged Fe–Mn–Al–C ($C \leqslant 1.3$) alloys [6]. However, the prevailing mechanisms leading to such exceptional combination of strength and ductility in the higher-carbon Fe–Mn–Al–C alloys remain to be clarified. In this study, we present a detailed analysis to unveil the unique microstructural features and strengthening mechanisms prevailing in the aged Fe–30Mn–9.5Al–2.0C alloy.

* Corresponding author. Tel.: +886 9 55108086; fax: +886 3 5713987.
E-mail address: tfliu@cc.nctu.edu.tw (T.-F. Liu).

0925-8388/$ - see front matter © 2013 Elsevier B.V. All rights reserved.
http://dx.doi.org/10.1016/j.jallcom.2013.10.153

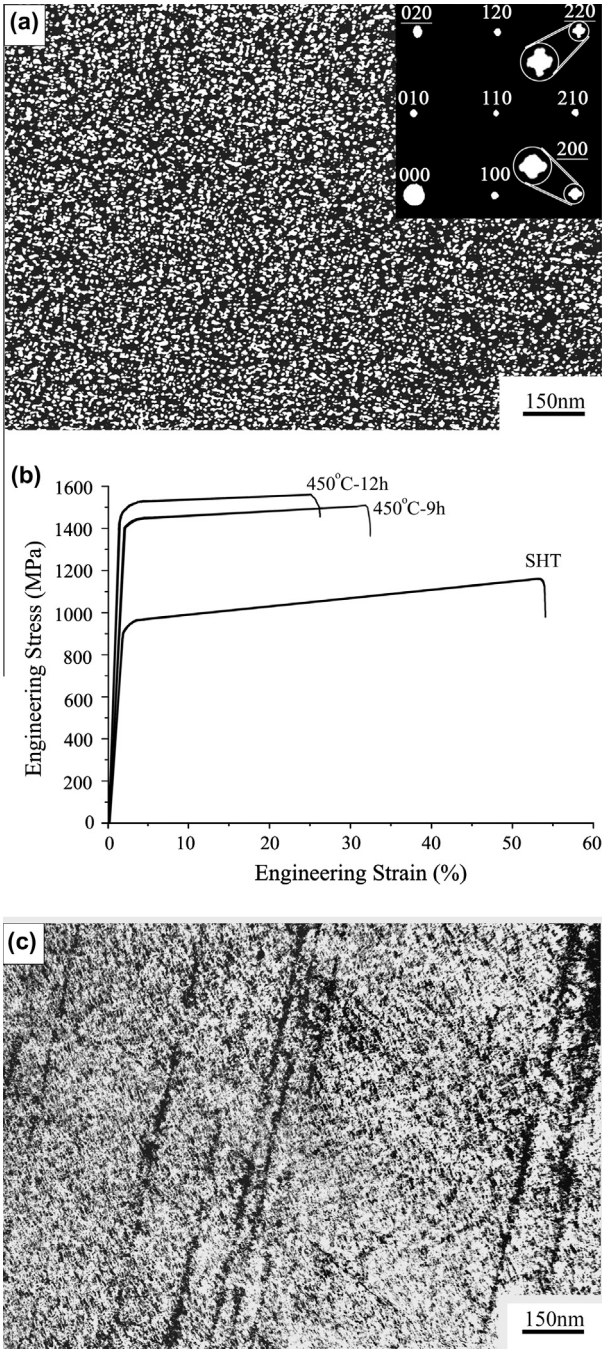

Fig. 1. (a) TEM $(100)_{\kappa'}$ dark-field image and the corresponding diffraction pattern (*hkl*: γ-phase, hkl: κ′-carbide) of the as-quenched alloy. (b) The engineering stress–strain curves for the alloy in the as-quenched condition and after being aged at 450 °C for 9 h and 12 h, respectively. (c) TEM bright-field image of the as-quenched alloy after tensile test, showing the presence of long slip lines.

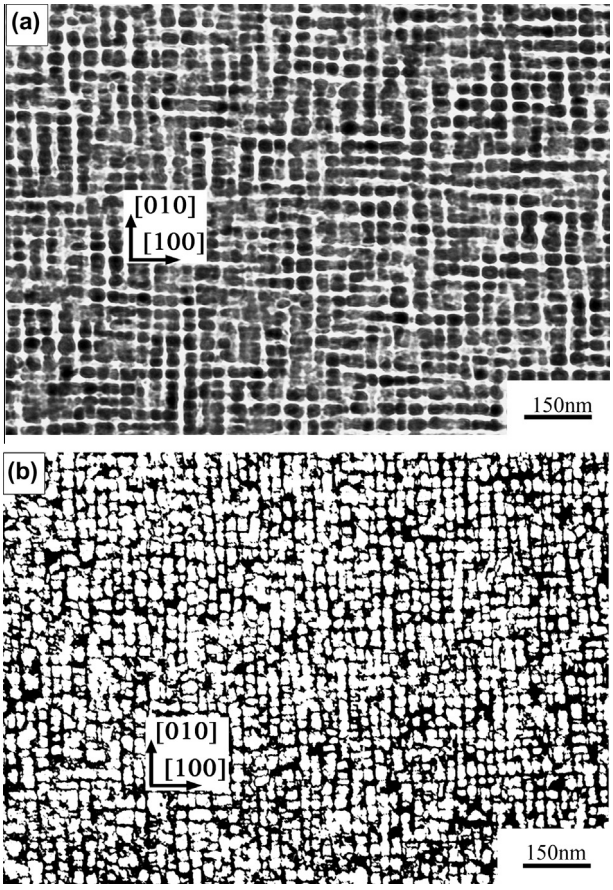

Fig. 2. TEM images of the alloy after being aged at 450 °C for 9 h: (a) bright-field image and (b) $(100)_{\kappa'}$ dark-field image. They were taken in [001] zone. Notice that the γ-phase nano-channels are nearly free of dislocations.

2. Experimental procedure

The nanostructured Fe–30Mn–9.5Al–2C alloy investigated in this study was prepared in an air induction furnace. After being homogenized at 1150 °C for 2 h under protective argon atmosphere, the ingot was hot-rolled to 6.5 mm-thick plate. The plate was subsequently solution heat-treated (SHT) at 1100 °C for 1 h and then quenched into room-temperature water. Aging processes were performed at 450 °C for 9–12 h. The specimens for tensile tests were prepared according to ASTM E8 standard having a gauge length of 50 mm, a gauge width of 12.5 mm and a thickness of 6 mm. Tensile tests were carried out at room-temperature with an Instron 8501 tensile testing machine at a strain rate of $6.7 \times 10^{-4}\ s^{-1}$. The YS was measured at 0.2% offset strain. The microstructures were analyzed by a JEOL-2100 transmission electron microscope (TEM) operating at 200 kV. A LECO2000 image analyzer was used to determine the size and volume fraction of the κ′-carbides.

3. Results and discussion

Fig. 1a is TEM $(100)_{\kappa'}$ dark-field image and the corresponding diffraction pattern of the as-quenched alloy, showing that an extremely high density of nano-sized κ′-carbides was formed within the γ matrix by spinodal decomposition during quenching [6–9]. The average size and volume fraction of the κ′-carbides in the as-quenched alloy are about 10 nm and 40%, respectively. Fig. 1b shows the tensile stress-strain curves of the as-quenched and aged alloys. The UTS, YS, and El of the as-quenched alloy are 1150 MPa, 950 MPa, and 53%, respectively. Fig. 1c shows the TEM observation of the as-quenched alloy after tensile test. It is evident that, since the size of the κ′-carbides is too tiny to completely obstruct dislocation gliding, long slip lines can be observed within the γ matrix. Consequently, in the as-quenched state, the deformation is dominated by the conventional dislocation impediment strengthening mechanisms.

The engineering stress–strain curves shown in Fig. 1b evidently indicate that, after being aged at 450 °C for 9 h and 12 h, the YS increases drastically up to 1406 MPa and 1452 MPa, while the total El are maintained at 32.1% and 26.3%, respectively. The results clearly demonstrate that, after being properly aged, the alloy can have far superior combination of strength and ductility to that of the Fe–Mn–Al–C ($C \leqslant 1.3$) alloys [2–5]. It's worthwhile to note that the yield strength and tensile strength are also slightly higher than those of the Fe–28Mn–9Al–1.8C alloy reported earlier by Chang et al. [6]. More significantly, a YS/UTS ratio of 94% is obtained. The striking features of possessing the exceptional combination of strength and ductility, as well as diminishingly small work

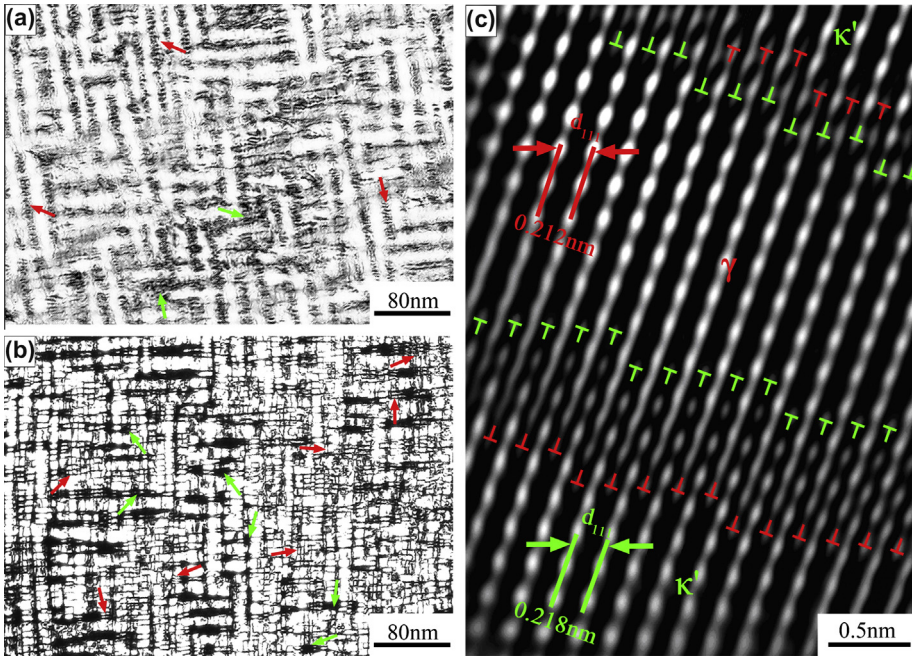

Fig. 3. TEM images of the aged (450 °C, 9 h) alloy after tensile test: (a) bright-field image, (b) $(100)_{\kappa'}$ dark-field image and (c) the lattice image, showing that the dislocations near the γ/κ′ interface are formed in pair-wise manner (indicated by the ⊥ and ⊤ dislocation symbols), a unique feature of Taylor lattice [20].

hardening rate in the aged alloys strongly suggest that the deformation mechanism must be very different from the conventional strengthening mechanisms [10,11]. Extensive microstructural analyses before and after tensile tests were thus performed to unveil the underlying deformation mechanisms prevailing in the present aged alloys.

Fig. 2a and b shows that, after being aged at 450 °C for 9 h, the nano-sized κ′-carbides grew along the ⟨100⟩ directions. The average size and volume fraction increased dramatically to become about 22 nm and 68%, respectively. Due to the substantially increased areal coverage of the κ′-carbides, the microstructure exhibits a very unique feature of well-divided isolated γ-phase nano-channels with dimensions of about 7–10 nm-wide and 40–100 nm-long bounded by grown κ′-carbides. The TEM analysis shown in Fig. 2a reveals that γ-phase nano-channels are nearly free of dislocations. The unique morphology of the isolated γ-phase nano-channels with nearly free of dislocations is believed to play a decisive role on the deformation behavior. It has been well-established that the deformation behavior in single crystal nano-pillars ranging from ∼50 to ∼1000 nm in diameter is dominated by "dislocation starvation strengthening mechanism" [12–18]. In this mechanism, the dislocation multiplication activities are largely suppressed due to the drastically reduced sample size and the flow stress is limited by dislocation nucleation. This is quite different from the conventional strengthening mechanisms for bulk materials and might have been prevailing in the present aged alloys. In our case here, the fact that the width of the isolated γ-phase nano-channels is only 7–10 nm and they are bounded by the grown directional κ′-carbides, which would result in an even more stringent condition for dislocation nucleation. Consequently, plastic deformation will not occur until the stress is sufficiently high to trigger the nucleation of new dislocations in the γ-phase nano-channels. This would give rise to the ultrahigh yield strength as observed in Fig. 1b. The results shown in Fig. 1b also indicate that the YS increased moderately from 1406 to 1452 MPa at the expense of substantially reduced elongation from 32.1% to 26.3% when the aging time was prolonged from 9 h to 12 h. This can be understood as being arisen from the reduced width of isolated γ-phase nano-channels due to the increased size and volume fraction of nano-sized κ′-carbides with increasing aging time. Nevertheless, it is noted that the strengthening mechanism observed in the present aged alloy is quite different from the six conventional strengthening mechanisms including solid solution strengthening, grain boundary strengthening, working hardening, precipitation or dispersion hardening, transformation strengthening and nano-twins [10,11].

Fig. 3a and b shows the TEM bright-field and $(100)_{\kappa'}$ dark-field images of the alloy aged at 450 °C for 9 h after tensile test, respectively. The bright-field image clearly reveals that no long slip lines could be observed and a very high density of dislocations homogeneously distributed within the γ-phase nano-channels as shown in Fig. 3a. Moreover, these dislocations are all oriented normal to the γ/κ′-carbide interfaces, as indicated by red arrows. The fact that the dislocations, instead of aligning along the orientations defined by the slip systems of the face-centered-cubic austenitic lattice, are running in the shortest distance within the γ-phase nano-channels, suggesting that these dislocations are newly nucleated through a bursting manner to effectively accommodate the plastic strain. From the energy considerations it would be expected that, in addition to minimum length of dislocation lines, the image stresses from the interface always tend to rotate the dislocation lines until they are normal to the surface [19]. Moreover, as the nucleation threshold is reached, the bursting dislocations within the isolated γ-phase nano-channels glide along the individual channel and interact with dislocations from adjacent γ-phase nano-channels at some of the channel intersections. This is evidently exhibited from the nano-sized slip traces and heavily strained intersection regions, as indicated by the red and green arrows in Fig. 3a and b, respectively. This also explains why only very limited work hardening rate is observed for the aged alloys as shown in Fig. 1b. Moreover, it is also noted that when the dislocation does glide through the shearable nano-sized κ′-carbides, it tends to split the κ′-carbides into even smaller size and form even narrower isolated γ-phase nano-channels, as indicated by the red arrows in Fig. 3b. An in-depth computational dislocation dynamics analysis is required to fully assess the dislocation behavior in the confined nano-channels.

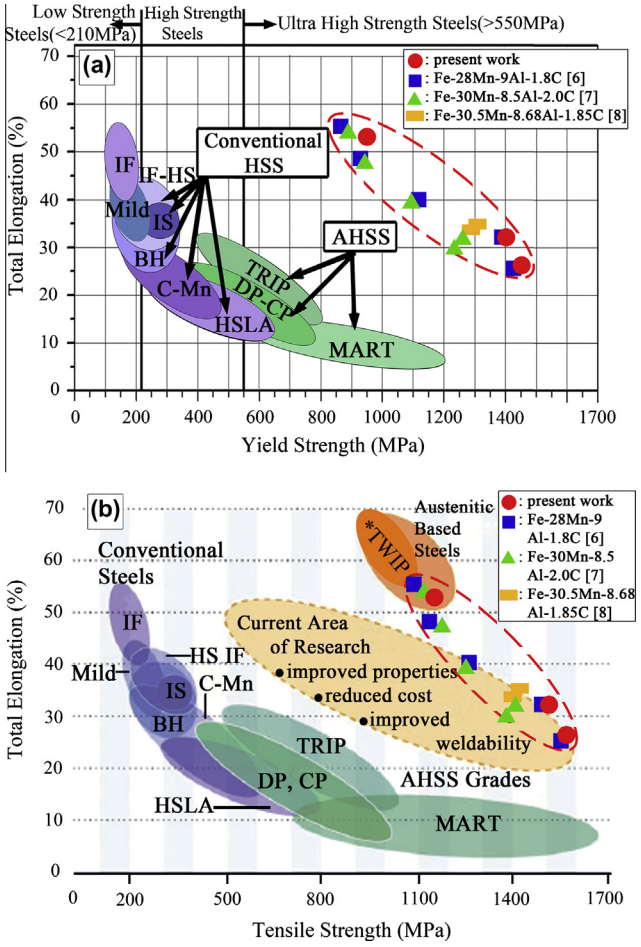

Fig. 4. (a and b) Shows the summary of the total elongation versus yield strength and ultimate tensile strength for the steels used in automotive industry over the past 50 years and the results obtained from the our current and previous work, respectively. The full name of acronyms appearing in the figure are interstitial-free (IF), isotropic steel (IS), bake hardenable (BH), carbon–manganese (C–Mn), high-strength low-alloy (HSLA), dual-phase (DP), complex-phase (CP), transformation-induced plasticity (TRIP), and martensite (MART), respectively.

It is also worth mentioning that the Taylor dislocation lattice could be observed at the γ/κ′-carbide interface in the present aged alloy as shown in the high-resolution TEM image (Fig. 3c). Obviously, these dislocations are distributed in a pair-wise manner (as marked by the dislocation symbols in Fig. 3c), which is one of the most prominent features of the Taylor dislocation lattice [20]. In such configuration, the stored energy is lowered by mutual screening and, hence, the maximum number of dislocations can be formed to homogeneously accommodate the strain up to a maximum level. To the best of our knowledge, Fig. 3c probably is the first direct evidence disclosing the very feature of Taylor lattice since it was proposed decades ago [20].

Finally, the mechanical properties obtained from the present work and the results obtained from our previous studies of Fe–Mn–Al–C alloys with higher carbon content and several other commercially available steels are summarized in Fig. 4a and b. Fig. 4 is a historical epitome summarizing the development of steels used in automotive industry over the last 50 years [11,21,22]. It is evident from Fig. 4 that both the conventional low- to high-strength steels and the first generation advanced high strength steels (1GAHSS) are primarily ferrite-based steels [22], in both the marked increase in strength is usually accompanied by a sharp reduction in ductility. For example, the martensitic steels although can have YS ~ 1200 MPa, their El has reduced to only 4%–6% [21]. A desire to produce steels with significantly higher ductility has led to the development of the second generation AHSS (2GAHSS) by adding 16–31 wt.% of Mn to obtain a fully austenitic (γ) microstructure at room-temperature. The representative examples of the 2GAHSS are the so-called twinning-induced plasticity (TWIP) Fe–Mn–Al–Si or Fe–Mn–C steels [22–25]. Although the TWIP steels can possess both excellent El (>50%) and high UTS (800–1100 MPa), they usually have relatively lower YS (~500 MPa) [21–25]. To bridge the gap of strength–elongation balance, the Steel Market Development Institute had put forth a "current area of research" for developing the third generation AHSS (3GAHSS) which is highlighted as the yellow area in Fig. 4b [11]. Evidently, the yield strength–ductility and tensile strength–ductility combinations of the present alloys, are superior to those of the 3GAHSS.

4. Conclusions

The deformation mechanisms of an ultrahigh-strength and high-ductility nanostructured Fe–30Mn–9.5Al–2.0C alloy have been investigated. Owing to the unique microstructure of isolated γ-phase nano-channels bounded by large volume fraction of highly directional κ′-carbides, the local plastic deformation in the aged alloy becomes dominated by bursting dislocation nucleation within the nano-channels. Such strengthening mechanism is completely different from the conventional ones and has never been observed in other bulk metallic materials. Consequently, the present aged alloy simultaneously exhibits an exceptional combination of ultra-high yield strength and excellent high ductility. Direct evidence of the Taylor dislocation lattice at the γ/κ′-carbide interfaces is also revealed, perhaps for the first time, in high-resolution TEM lattice image.

Acknowledgements

This work was supported by National Science Council, Republic of China under Grant NSC100-2221-E-009-053-MY3. JYJ is partially supported by MOE-ATU program operated at NCTU.

References

[1] J. Jeong, C.Y. Lee, I.J. Park, Y.K. Lee, Isothermal precipitation behavior of κ-carbide in the Fe–9Mn–6Al–0.15C lightweight steel with a multiphase microstructure, J. Alloys Comp. 574 (2013) 299–304.
[2] W.K. Choo, J.H. Kim, J.C. Yoon, Microstructural change in austenitic Fe–30.0 wt%Mn–7.8 wt%Al–1.3 wt%C initiated by spinodal decomposition and its influence on mechanical properties, Acta Mater. 45 (1997) 4877–4885.
[3] I. Kalashnikov, O. Acselrad, A. Shalkevich, L.C. Pereira, Chemical composition optimization for austenitic steels of the Fe–Mn–Al–C system, J. Mater. Eng. Perform. 9 (2000) 597–602.
[4] K.T. Park, Tensile deformation of low-density Fe–Mn–Al–C austenitic steels at ambient temperature, Scr. Mater. 68 (2013) 375–379.
[5] I. Gutierrez-Urrutia, D. Raabe, Influence of Al content and precipitation state on the mechanical behavior of austenitic high-Mn low-density steels, Scr. Mater. 68 (2013) 343–347.
[6] K.M. Chang, C.G. Chao, T.F. Liu, Excellent combination of strength and ductility in an Fe–9Al–28Mn–1.8C alloy, Scr. Mater. 63 (2010) 162–165.
[7] C.L. Lin, C.G. Chao, H.Y. Bor, T.F. Liu, Relationship between microstructures and tensile properties of an Fe–30Mn–8.5Al–2.0C Alloy, Mater. Trans. 51 (2010) 1084–1088.
[8] P.C. Chen, C.G. Chao, T.F. Liu, A novel high-strength, high-ductility and high-corrosion-resistance FeAlMnC low-density alloy, Scr. Mater. 68 (2013) 380–383.
[9] G.D. Tsay, Y.H. Tuan, C.L. Lin, C.G. Chao, T.F. Liu, Effect of carbon on spinodal decomposition in Fe–26Mn–20Al–C alloys, Mater. Trans. 52 (2011) 521–525.
[10] K. Lu, L. Lu, S. Suresh, Strengthening materials by engineering coherent internal boundaries at the nanoscale, Science 324 (2009) 349–352.
[11] C.M. Tamarelli, Steel market Development Institute, AHSS 101: The Evolving Use of Advanced High-Strength Steels for Automotive Applications, 2011, <http://www.autosteel.org>, [edition]
[12] M.D. Uchic, D.M. Dimiduk, J.N. Florando, W.D. Nix, Sample dimensions influence strength and crystal plasticity, Science 305 (2004) 986–989.

[13] J.R. Greer, W.D. Nix, Nanoscale gold pillars strengthened through dislocation starvation, Phys. Rev. B 73 (2006) 245410.
[14] Z.J. Wang, Q.J. Li, Z.W. Shan, J. Li, J. Sun, E. Ma, Sample size effects on the large strain bursts in submicron aluminum pillars, Appl. Phys. Lett. 100 (2012) 071906.
[15] G. Richter, K. Hillerich, D.S. Gianola, R. Mönig, O. Kraft, C.A. Volkert, Ultrahigh strength single crystalline nanowhiskers grown by physical vapor deposition, Nano Lett. 9 (2009) 3048–3052.
[16] Z.W. Shan, R.K. Mishra, S.A. Syed Asif, O.L. Warren, A.M. Minor, Mechanical annealing and source-limited deformation in submicrometre-diameter Ni crystals, Nat. Mater. 7 (2008) 115–119.
[17] A. Jérusalem, A. Fernández, A. Kunz, J.R. Greer, Continuum modeling of dislocation starvation and subsequent nucleation in nano-pillar compressions, Scr. Mater. 66 (2012) 93–96.
[18] J.R. Greer, Bridging the gap between computational and experimental length scales: a review on nanoscale plasticity, Rev. Adv. Mater. Sci. 13 (2006) 59–70.
[19] J.P. Hirth, J. Lothe, Theory of Dislocations, McGraw-Hill Inc., New York, 1968.
[20] D. Kuhlmann-Wilsdorf, Theory of plastic deformation: -properties of low energy dislocation structures, Mater. Sci. Eng. A 113 (1989) 1–41.
[21] WorldAutoSteel, Advanced High Strength Steel (AHSS) Application Guidelines Version 4.1, 2009, <http://www.autosteel.org>, [edition].
[22] D.K. Matlock, J.G. Speer, Third generation of AHSS: microstructure design concepts, in: A. Haldar, S. Suwas, D. Bhattacharjee (Eds.), Microstructure and Texture in Steels, Springer London, India, 2009, pp. 185–205 (Chapter 11).
[23] O. Grässel, L. Krüger, G. Frommeyer, L.W. Meyer, High strength Fe–Mn–(Al, Si) TRIP/TWIP steels development-properties-application, Int. J. Plasticity 16 (2000) 1391–1409.
[24] S. Curtze, V.-T. Kuokkala, Dependence of tensile deformation behavior of TWIP steels on stacking fault energy, temperature and strain rate, Acta Mater. 58 (2010) 5129–5141.
[25] K.G. Chin, C.Y. Kang, S.Y. Shin, S. Hong, S. Lee, H.S. Kim, K.H. Kim, N.J. Kim, Effects of Al addition on deformation and fracture mechanisms in two high manganese TWIP steels, Mater. Sci. Eng. A 528 (2011) 2922–2928.